International Journal of Multiphase Flow 112 (2019) 116–129

Contents lists available at ScienceDirect

International Journal of Multiphase Flow

journal homepage: www.elsevier.com/locate/ijmulflow

Turbulence modulation by finite-size spherical particles in Newtonian and viscoelastic fluids

Sagar Zade*, Fredrik Lundell, Luca Brandt

Linné Flow Centre and SeRC (Swedish e-Science Research Centre), KTH Mechanics, SE 100 44 Stockholm, Sweden

ARTICLE INFO

Article history:
Received 26 September 2018
Revised 15 December 2018
Accepted 17 December 2018
Available online 18 December 2018

Keywords:
Turbulent flow
Newtonian fluid
viscoelastic fluid
drag reduction
particle-laden flow

ABSTRACT

We experimentally investigate the influence of finite-size spherical particles in turbulent flows of a Newtonian and a drag reducing viscoelastic fluid at varying particle volume fractions and fixed Reynolds number. Experiments are performed in a square duct at a Reynolds number Re_{2H} of nearly 1.1×10^4, Weissenberg number Wi for single phase flow is between 1 and 2 and results in a drag-reduction of 43% compared to a Newtonian flow (at the same Re_{2H}). Particles are almost neutrally-buoyant hydrogel spheres having a density ratio of 1.0035 ± 0.0003 and a duct height $2H$ to particle diameter d_p ratio of around 10. We measure flow statistics for four different volume fractions ϕ namely 5, 10, 15 and 20% by using refractive-index-matched Particle Image Velocimetry (PIV). For both Newtonian Fluid (NF) and Visceolastic Fluid (VEF), the drag monotonically increases with ϕ. For NF, the magnitude of drag increase due to particle addition can be reasonably estimated using a concentration dependent effective viscosity for volume fractions below 10%. The drag increase is, however, underestimated at higher ϕ. For VEF, the absolute value of drag is lower than NF but, its rate of increase with ϕ is higher. Similar to particles in a NF, particles in VEF tend to migrate towards the center of the duct and form a layer of high concentration at the wall. Interestingly, relatively higher migration towards the center and lower migration towards the walls is observed for VEF. The primary Reynolds shear stress reduces with increasing ϕ throughout the duct height for both types of fluid.

1. Introduction

Turbulent flow of suspensions is encountered in many natural situations e.g. transport of sediments, flow of red blood cells in the body, etc. and industrial applications e.g. transport of crushed coal, slurries, particle dispersions in paints, foodstuffs, etc. This article focuses on a suspension of spherical particles in a square duct. Turbulent characteristics of the single phase flow are modified to varying extents based on particle size (Costa et al., 2018), shape (Ardekani et al., 2017), concentration (Lashgari et al., 2014), density ratio (Fornari et al., 2016) and deformability (Alizad Banaei et al., 2017). Velocity and particle distribution determine the friction at the wall which is of fundamental importance in estimating power consumption in process industries.

Suspension of finite-size particles in wall-bounded Newtonian flows have been shown to exhibit a variety of rich physics. In the viscous Stokes regime, particles migrate from regions of high shear to low shear due to irreversible interactions, e.g. towards the centerline in a Poiseuille flow (Guazzelli and Morris, 2011). With an increase in particle Re, inertial effects become important and particles tend to move away from the centerline and equilibrate at an intermediate position due to the repulsive forces from the wall (see the tubular pinch effect in Segré and Silberberg (1962)). Dilute laminar flow of finite-size particles is known to exhibit an increase in the effective viscosity (Guazzelli and Morris, 2011). Bagnold (1954) showed how inter-particle collisions increase the effective viscosity in the highly inertial regime. Such inertial effects at the particle scale can induce other rheological effects like shear-thickening (Picano et al., 2013). Lashgari et al. (2014) showed how the distribution of viscous, turbulent and particle stresses varies when changing the particle volume fraction and the Re in a plane channel flow. For a square duct, Kazerooni et al. (2017) studied numerically the suspension of laminar flow at different Re, up to a particle volume fraction $\phi = 20\%$, and for different duct to particle size ratios. According to their study, particles largely move to the corners at lower volume fractions and at higher Re. Fornari et al. (2018a) investigated turbulent flows of a suspension of spherical rigid particles in a square duct up to a volume fraction of 20% and found that at the highest volume fraction, particles preferentially accumulate in the core region and the intensity of the secondary flows reduces below that of the unladen case.

* Corresponding author.
E-mail address: zade@mech.kth.se (S. Zade).

https://doi.org/10.1016/j.ijmultiphaseflow.2018.12.015
0301-9322/

It is well known that addition of trace amounts, e.g. few parts per million, of long-chain polymer into a (soluble) solution leads to a remarkable decrease in the wall friction, referred to as Tom's effect (Toms, 1948). This drag reduction capability has been successfully used in crude-oil pipelines for increasing the flow rate at fixed pumping costs, the most famous example being the Trans Alaskan Pipeline in 1979 (Burger et al., 1980), in preventing flooding by increasing the discharge of sewage during excessive rainfall (Sellin and Ollis, 1980), district heating and cooling (Leca and Leca, 1984), etc. Polymer additives are particularly attractive for industrial applications since only minute quantities can have substantial drag-reducing effect.

These high molecular polymers dissolve in the solvent liquid and form coiled microstructures that have elastic properties and thus the resulting solution is viscoelastic in its rheology. When the relaxation time λ of these microstructures is comparable or larger than the characteristic deformation time of the flow $1/\dot{\epsilon}$, $\dot{\epsilon}$ being the extensional strain rate, these coiled microstructures stretch and substantially increase the elongational viscosity of the solution. The increased elongational viscosity, which mostly occurs in the near-wall region, where $\dot{\epsilon}$ is the highest, suppresses turbulent fluctuations. The effectiveness of polymer solutions, thus, depends on the stretching of individual molecules by the stresses in the flow (Gyr and Bewersdorff, 2013). The Weissenberg number *Wi*, given by $\lambda\dot{\epsilon}$, compares the elastic forces to the viscous forces in the fluid.

With increasing drag reduction, there is an increase in the spanwise spacing between the low-speed velocity streaks and there is a reduction in the number and strength of near-wall vortical structures while their size also increases (White et al., 2004). Turbulence is attenuated at small scales due to the increasing elastic energy stored in the stretched coils at the small scales (owing to higher stretching dynamics at small scales), thus interfering with the usual turbulence cascade mechanism (Sreenivasan and White, 2000). Reynolds shear stress is substantially reduced leading to a reduction in cross-stream momentum transfer. The drag reduction is ultimately bounded by the maximum drag reduction asymptote (Virk, 1975) where the Reynolds shear stress reduces to nearly zero but, turbulence is sustained because of the interaction between fluctuating polymer stresses and the fluctuating velocity gradient (Warholic et al., 1999). Also see Hara et al. (2017), who experimentally studied the Reynolds number dependency of this interaction term. Amongst the many proposed mechanisms for regeneration of polymer wall turbulence, Dubief et al. (2004) found that polymer chains extract energy from the near-wall vortices ($y^+ \geq 20$) as they are pulled around the vortices, and release energy in the high speed streaks that are located just above the viscous sublayer ($y^+ \approx 5$) thus, causing an autonomous regeneration cycle.

Regarding VEF flow in a square duct, Gampert and Rensch (1996) found that with increasing polymer concentration in a square duct, the axial turbulence intensity first increases and then decreases even below the level obtained with a pure solvent. Escudier and Smith (2001) performed detailed spatial measurements of mean axial and secondary flow velocity as well as turbulence statistics for various polymer solutions in the duct. They found that apart from a reduction in the transverse turbulence intensity, there is also a strong reduction in the secondary flow velocities. Owolabi et al. (2017) measured drag reduction in turbulent flow through ducts of various cross-sections and at varying degrees of mechanical degradation of polymer molecules. They found that the drag reduction, at least for flexible linear polymer additives, is a function of the *Wi* (estimated using the fluid relaxation time λ and the mean shear rate at the wall) only. Shahmardi et al. (2019) performed direct numerical simulations (DNS), using the FENE-P model, to study the modulation of secondary flow. They found that, compared to NF case, the counter rotating vortices become larger and their centers are displaced towards the center of the duct away from the walls.

In many industrial processes, e.g. food-processing, particles are suspended in a VEF medium. In addition, considering the high effectiveness of drag reducing polymer additives in single phase flow, it is of practical importance to assess their effectiveness in a suspension flow. However, studies in this field mostly deal with the motion of inertia-less particles passively transported in VEF (see Nowbahar et al., 2013 and review by D'avino and Maffettone (2015)). For finite-size particles in VEF, very few studies exists and even those are mostly related to motion of a single particle at low *Re*. Van den Brule and Gheissary (1993) found that settling velocity of a spherical particle is reduced by elastic effects (e.g. presence of normal stress differences and high elongational viscosity) in the fluid, and that this effect becomes significantly higher with increasing shear rates experienced by the falling sphere. Michele et al. (1977) observed alignment and aggregation of spheres in plane shear flows. Li et al. (2015) numerically studied the migration of a sphere in laminar square duct flow and found that the equilibrium position depends on the interplay between the elastic (driving the particle towards the channel center line) and inertial effects (drives the particle away from the channel center line). Also shear-thinning effects and secondary flows tend to move the particle away from the channel center line. Dramatic reduction in particle mobility, i.e. the tensor of proportionality between applied force and particle velocity, is seen due to viscoelastic wake structures, that are linked to an increase in the form drag (Murch et al., 2017). Recently, Einarsson et al. (2018) analytically calculated the suspension stress for a dilute suspension of spheres in a viscoelastic medium and showed how shear-thickening arises from strain 'hot spots' in the disturbance flow around particles.

Most of the studies in suspension flows are performed using numerical tools because of its ability to provide spatiotemporally resolved data which can shed light on the phyiscal mechanism behind the bulk observables. High performance computers have made possible fully resolved DNS at moderate Reynolds number. Using Immersed Boundary Method (IBM) of forcing, where the particle geometry is resolved, it has been possible to capture fluid-particle interaction with high fidelity (Breugem, 2012). However, to our knowledge, such a coupling has not been extended to suspension of turbulent viscoelastic flow. Experiments, on the other hand, are quite challenging due to lack of a convenient measurement techniques where both time and spatially resolved data can be acquired. Optical techniques fail with opaque particles where it becomes impossible to *see* in the core of the flow. Refractive index matched particles have been used with quite some success to overcome this hurdle (Wiederseiner et al., 2011; Byron and Variano, 2013; Klein et al., 2012; Zade et al., 2018) and have been used in this study.

1.1. Outline

In this study, we perform experiments with a suspension of spherical particles in a Newtonian fluid (NF) as well as a drag reducing viscoelastic fluid (VEF). The wall-bounded geometry is a square duct and measurements are performed in the center-plane i.e. the plane of the wall-bisector. In order to make a consistent comparison for both types of fluid flows, the Reynolds number is kept constant $Re_{2H} = 1.1 \times 10^4$. We study the change in wall friction and turbulent velocity statistics as a function of the particle volume fraction. By being able to differentiate between the fluid and particle phase, it is also possible to measure the mean particle concentration and velocity profile in the measurement plane.

In the following sections we first describe the experimental set-up and the measurement techniques along with information

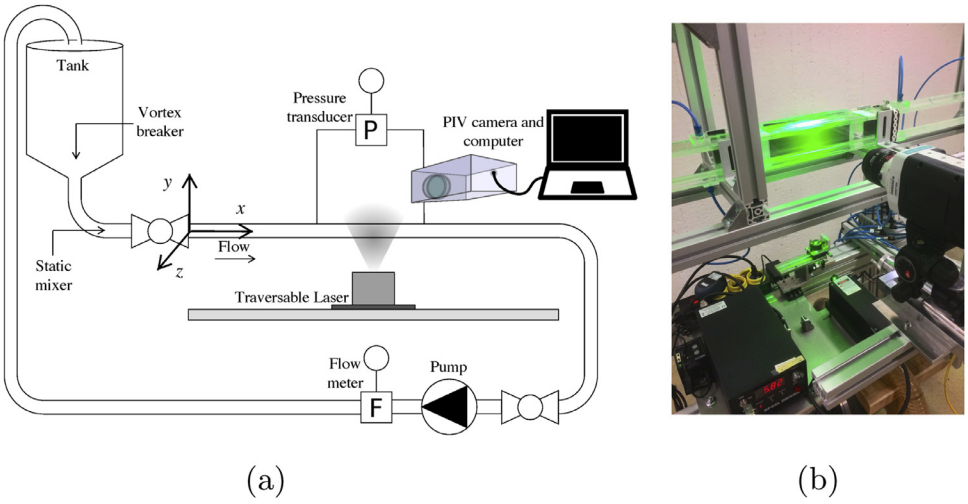

Fig. 1. (a) Schematic of the flow-loop (b) Photo of the section where PIV is performed.

pertaining to particles and the rheology of the VEF. Later we present results, first with particles in NF and later in VEF. Finally we conclude by comparing the most interesting differences between suspension in the two fluid types.

2. Experimental technique

2.1. Experimental set-up

The experiments were performed in a transparent Plexiglas square duct that is 50 mm x 50 mm in cross section and 5 m in length. Fig. 1a shows a schematic of the flow loop. The fluid is recirculated through a conical tank that is open to the atmosphere, where the particle-fluid mixture can be introduced. A tripping tape is lined on the inner walls of the Plexiglas duct at the inlet to trigger turbulence. The temperature of the solution is maintained at nearly 20°C by means of an external heat-exchanger in the tank. A gentle disc pump (Discflo Corporations, CA, USA) has been chosen to minimize mechanical breakage of the particles. It can pump rather large particles at reasonably high volume concentration without pulsations. Additional details about the set-up can be found in Zade et al. (2018).

An electromagnetic flowmeter (Krohne Optiflux 1000 with IFC 300 signal converter, Krohne Messtechnik GmbH, Germany) is used to measure the flow rate. The Reynolds number Re_{2H}, used hereafter, is based on the average or bulk velocity U_{Bulk} of the fluid-particle mixture, the viscosity of the fluid η and full height of the duct $2H$. The pressure drop is measured across a length of $54H$ in a region of the duct that is nearly $140H$ from the inlet (the turbulent flow was seen to be fully developed at this entry length) using a differential pressure transducer (0 - 1 kPa, Model: FKC11, Fuji Electric France, S.A.S.). Fig. 2 shows a reasonable agreement between the friction-factor $f = \tau_w/(\rho_f U_{Bulk}^2/2)$ for the single phase Newtonian fluid flow measured in our square duct and the empirical correlation given in Duan et al. (2012),

$$f = \left(3.6\log_{10}\left(\frac{6.115}{Re_{\sqrt{A}}}\right)\right)^{-2}. \quad (1)$$

Here, $\tau_w = (dP/dx)(H/2)$ is the wall shear stress measured from the streamwise pressure gradient dP/dx and ρ_f is the density of the fluid. The Reynolds number $Re_{\sqrt{A}}$ in Eq. (1) is based on the characteristic length given by the square root of the cross section area $A = 2H \times 2H$. The friction velocity, used later, is given by $u_\tau = \sqrt{\tau_w/\rho_f}$. Data acquisition from the camera, flow meter and pressure transducer is performed using a National Instruments NI-6215 DAQ card using Labview™ software.

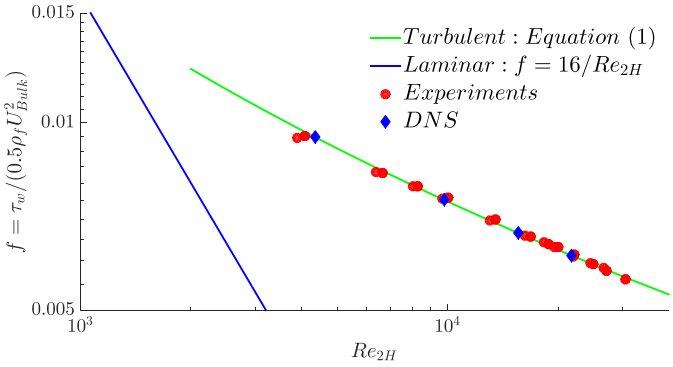

Fig. 2. Comparison between experiments, DNS simulations from Zhang et al. (2015) and empirical correlation for the Fanning friction factor f as a function of bulk Reynolds number Re_{2H} for single-phase Newtonian fluid.

2.2. Particle properties

The finite-size particles are commercially procured super-absorbent (polyacrylamide based) hydrogel. Once mixed with water and left submerged for nearly 24 h at room temperature, they grow to an equilibrium size of 5 ± 0.8 mm. To enhance the contrast of the particles in the PIV images, a small amount of Rhodamine is added to the water in which the particles expand. The particle size is determined by a digital imaging system as well as from the PIV images. The fact that a Gaussian like particle size distribution, with small variance, has small effect on the flow statistics has been shown in Fornari et al. (2018b).

The density of the particles is determined by (i) measuring the volume displaced by a known mass of particles and (ii) by determining the terminal settling velocity in a long liquid settling column. In the first method, a known mass of fully expanded particles was put in a water-filled container of uniform diameter. The rise in the level of water due to the particles was measured using a very precise laser distance meter (optoNTDC 1710, Micro-Epsilon Messtechnik GmbH, resolution = 0.5 µm). In the second method, a single particle with a known diameter was gently dropped in a long vertical pipe, filled with water, wide enough so as to minimize the wall effects. The relation for drag force F on a settling

particle in Crowe et al. (2011),

$$\frac{F}{\rho_f U_T^2 A} = \frac{12}{Re_p}(1 + 0.15 Re_p^{0.687}) \quad (2)$$

applicable in the transitional regime: $1 < Re_p < 750$, is used to relate the particle diameter d_p and terminal velocity U_T to the unknown particle density ρ_p. Here, A is the projected area of the particle and Re_p is the particle Reynolds number given by $\frac{\rho_p U_T d_p}{\mu_f}$ where, μ_f is the dynamic viscosity of the liquid. The measurements were repeated multiple times at a room temperature of around 20°C and both methods yielded a particle to fluid density ratio $\rho_p/\rho_f = 1.0035 \pm 0.0003$. Visualization of high-speed movies of the particles in flow, even at the highest concentrations, displayed no observable particle deformation. In this sense, the particles can be considered to be rigid. However, the extent to which the results may vary by using perfectly rigid particles, which may have different material dependent coefficient of friction, has not been assessed. The mechanical properties of commercially available spherical hydrogel particles are discussed in Dijksman et al. (2017).

For experiments in NF, if pure water is used as the suspending fluid, the particle density ratio is nearly equal to one, suggesting neutrally-buoyant particles i.e. the influence of gravity on the particle motion is negligible. However, at $Re_{2H} \approx 11000$, some sedimentation effects were visible in water. This can be quantified by calculating the Rouse number $Ro = U_T/\kappa u_\tau$ (Rouse, 1937), which is used to estimate whether the particles move as a bed load ($Ro \geq 2.5$) or in full suspension ($Ro \leq 1.2$) (Fredsøe and Deigaard, 1992). Here κ is the von Kármán constant taken to be equal to 0.41. For water, at a $Re_{2H} \approx 11000$, the $Ro \approx 2.4$, which leads to settling. Hence, to ensure that particles are in full suspension at the given Re_{2H}, it is necessary to increase the U_{Bulk} and to ensure that the Re_{2H} does not increase, thus the viscosity needs to be proportionately increased. This is accomplished by adding 3.6% by mass of low molecular weight (MW = 8000) Polyethylene Glycol (PEG) (Carbowax™, Fischer Scientific) to water which resulted in a transparent Newtonian solution with a viscosity that is 2.2 times the viscosity of water and $Ro \approx 0.8$ which corresponds to particles in full suspension at a $Re_{2H} \approx 11000$.

2.3. Polymer rheology

The VEF solution was prepared by adding 250 ppm of a high molecular weight polyacrylamide based anionic polymer (FLOPAM AN934SH, SNF, Molecular weight $> 15 \times 10^6$) to water. Being a commercial polymer, some degree of polydispersity is to be expected. Also polymer degradation during mixing and pumping would lower the number of high molecular weight chains. The density of the solution is practically the same as the solvent (water) under such dilute concentrations. The solution was prepared by dissolving the polymer in powder form to water, followed by successive dilution and mixing to ensure its homogeneity. Such a solution with the desired polymer concentration was stored in a large reservoir from which it was pumped to the tank at the beginning of every new experiment. The solution is recirculated for a long time in the flow loop so that the rheological properties were not changing much and the drag reduction has reached a nearly constant value. Thus, the polymers are degraded enough so that steady state PIV measurements are possible but, the level of drag reduction is lower than what is expected from a freshly prepared solution. The shear viscosity of the polymer solution was measured using a rheometer (Kinexus pro+, Malvern Panalytical). The variation of dynamic viscosity with shear rate is shown in Fig. 3 and shear thinning behavior can be clearly observed. It is known that only shear-thinning by itself produce no drag-reduction and hence, viscoelasticity is important (Metzner and Park, 1964). From

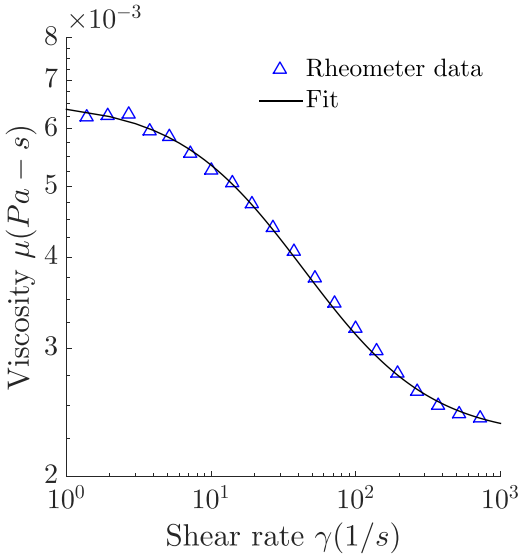

Fig. 3. Variation of viscosity with shear rate for the viscoelastic fluid.

the study of Owolabi et al. (2017), who used the same type and concentration of polymer additive as in this study, it can be said that the present level of drag reduction (at the same mass flow rate) corresponds to a Wi between 1and 2 and the corresponding fluid relaxation time $\lambda \approx 6.5$ ms. For this non-Newtonian fluid, the Reynolds number $Re_{2H} = U_{Bulk} 2H/\eta_w$, where η_w is the near-wall viscosity which corresponds to the average experimental shear stress (or equivalently shear rate) obtained from the pressure drop measurements in the fully developed region of the duct.

2.4. Velocity measurement technique

The coordinate system used in this study is indicated in Fig. 1a with x the streamwise, y the wall-normal and z the spanwise directions. The velocity field is measured using 2D Particle Image Velocimetry (2D-PIV) in the plane of the wall-bisector: $z/H = 0$. Thus, the two lateral walls are situated at $z/H = -1$ and 1 respectively. These measurements are performed at a streamwise distance of $x/H \approx 150$ from the entrance of the duct. A continuous wave laser (wavelength = 532 nm, power = 2 W) and a high-speed camera (Phantom Miro 120, Vision Research, NJ, USA) are used to capture successive image pairs. The thickness of the laser light-sheet is 1 mm. Fig. 1b shows a photo of the PIV set-up. For imaging the full height of the duct, a resolution of approximately 60 mm/1024 pixels is chosen. The frame rate (acquisition frequency) is selected such that the maximum pixel displacement does not exceed a quarter of the size of the final interrogation window IW (Raffel et al., 2013). Images are processed using an in-house, three-step, FFT-based, cross-correlation algorithm (Kawata and Obi, 2014). The final size of the IW is 32 × 32 pixel. The degree of overlap can be estimated from the fact that the corresponding final resolution is 1 mm x 1 mm per IW. Each experiment has been repeated at least 2 times and 500 image pairs, each separated by more than 4 flow turn-over time $T = 2H/U_{Bulk}$ so as to ensure statistically independent samples, have been observed to be sufficient for statistically converged results both for single phase and particle-laden flows.

Fig. 4 depicts one image from a typical PIV sequence for particle-laden flow. Raw images captured during the experiment are saved in groups of two different intensity levels. The first group of images (an example being Fig. 4a) is used for regular PIV processing according to the algorithm mentioned above. The second group of images (cf. Fig. 4b) are contrast-enhanced, e.g. they

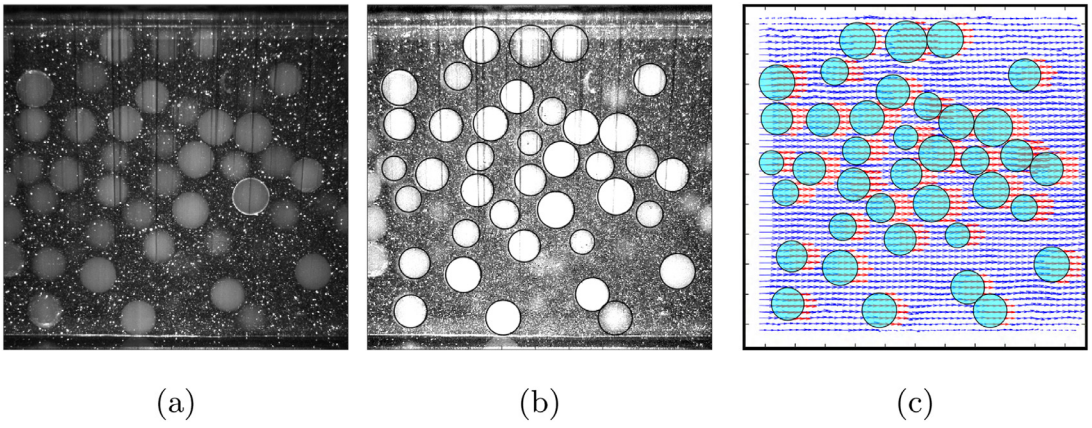

Fig. 4. (a) Image for PIV analysis, (b) image for particle detection and PTV analysis and (c) combined fluid PIV - particle PTV velocity vectors for $\phi = 20\%$.

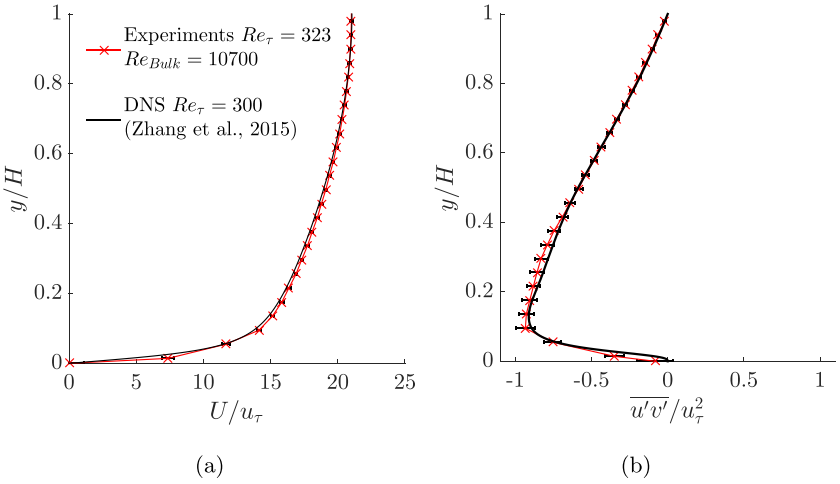

Fig. 5. Single phase Newtonian fluid (NF): (a) mean stream-wise velocity profiles and (b) Reynolds shear stress in the plane of the wall-bisector compared with the DNS simulations of Zhang et al. (2015) at a slightly lower Re_τ.

are sharpened and their intensity adjusted, and used for detecting the finite-size particles only using a circular Hough transform (Yuen et al., 1990). From the detected particles in image A and B of the PIV sequence, a nearest neighbor approach is used to determine their translational motion. Particles that are detected only in one image of the pair are, thus, eliminated by the PTV algorithm. For the Eulerian PIV velocity field, we define a mask, which assumes the value 1 if the point lies inside the particle and 0, if it lies outside. The fluid phase velocity is thus determined on a fixed mesh. The particle velocity is determined using PTV at its center, which is assigned to the grid points inside the particle (mask equal to 1). The velocity field of the particle-phase is, now, available at the same grid points as that of the fluid and the ensemble averaging, reported later, are phase averaged statistics. Fig. 4c shows the combined fluid (PIV) and particle (PTV) velocity field. A point to note is that, using the above PTV approach, we could measure the translational velocity of the particle but particle rotation could not be measured.

3. Results

3.1. Single phase flow

Fig. 5 shows the mean streamwise velocity profile and the Reynolds shear stress in the plane of the wall-bisector for single phase flow of NF at $Re_{2H} = 10700 \pm 100$ which corresponds to $Re_\tau = 323 \pm 6$. Only the bottom half is shown due to symmetry. Error bars with a width of two standard deviations are also plotted for the experimental data. Comparison with DNS simulations of Zhang et al. (2015) at a slightly lower $Re_\tau = 300$ shows reasonable agreement both in terms of mean velocity and correlation of fluctuating velocity components.

Addition of polymer additives introduces elasticity in the fluid phase and modifies the flow and overall drag and velocity statistics. For nearly the same $Re_{2H} = 10200 \pm 100$, drag for the single phase VEF flow is $43 \pm 2\%$ lower than for the single phase NF. Using the maximum drag reduction asymptote (Virk, 1975), the drag reduction at this Re_{2H} is expected to be around 66–69%. So, the present level of drag reduction is lower than the maximum drag reduction achievable. Drag change is calculated as the relative change in friction factor f as compared to friction factor of single phase Newtonian flow $f_{Sp,\,NF}$, at the same Re_{2H} and is given by

$$Relative\ drag\ modification = \left(100 \times \frac{f_{Sp,NF} - f}{f_{Sp,NF}}\right)_{Re_{2H}=constant} \quad (3)$$

The drag variation for the particle-laden cases is estimated in the same way. Fig. 6 shows the turbulent velocity statistics of single phase NF and VEF. The mean streamwise velocity, scaled in inner units, is shown in Fig. 6a. The average u_τ is measured from the pressure drop, and the wall-normal distance y is scaled using η_w/u_τ, where η_w is the viscosity corresponding to the average shear stress at the wall, as mentioned before. Virk's ultimate profile corresponding to the Maximum Drag Reduction (MDR)

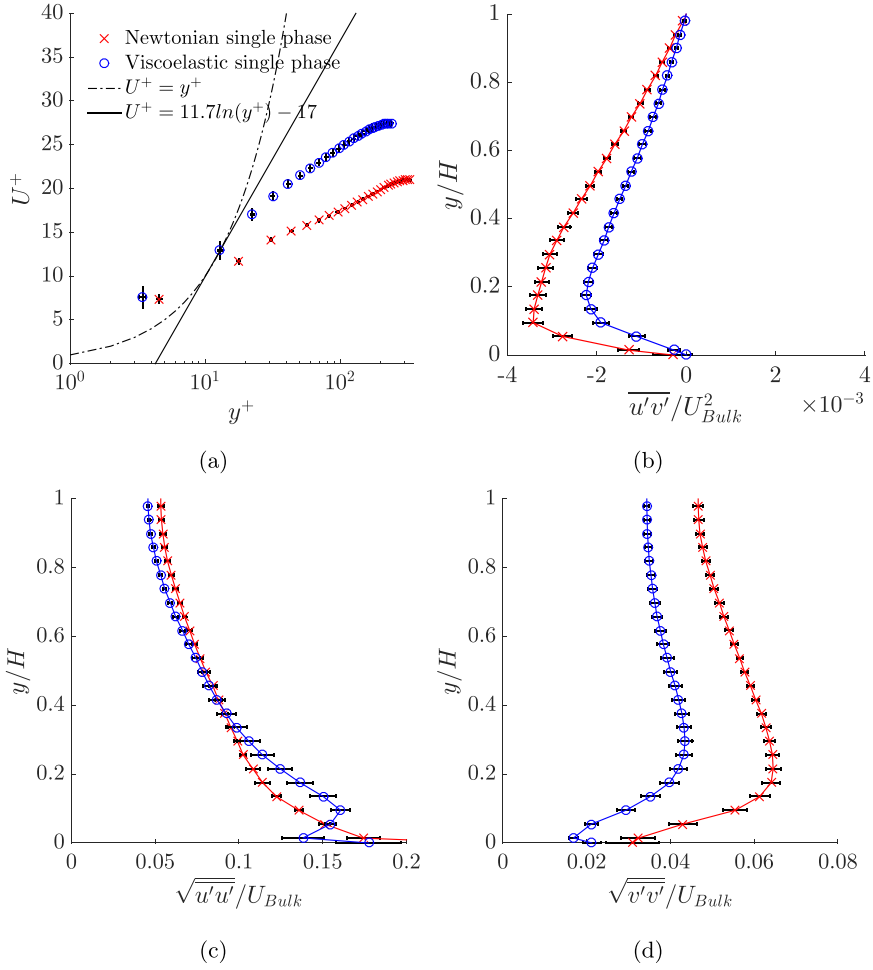

Fig. 6. Comparing single phase NF and VEF flow: (a) mean stream-wise velocity profiles, (b) Reynolds shear stress and fluid velocity fluctuations in the (c) stream-wise and (d) wall-normal directions in the plane of the wall-bisector.

asymptote (Virk, 1975) is also shown. The velocity profile is shifted upwards with a slightly higher slope than the Newtonian case in the log-region. Our resolution close to the wall is not sufficient to collapse data on $U^+ = y^+$ in the viscous sub-layer $y^+ \leq 5$. The mean streamwise velocity if scaled in bulk units (shown later in Fig. 12a) does not show any major differences compared to the Newtonian case, except in the near-wall region where the NF is slightly faster due to the higher level of turbulent mixing driven by the corresponding higher Reynolds shear stress, see Fig. 6b, which shows that the streamwise and wall-normal fluctuations are less correlated for turbulent VEF. The streamwise velocity fluctuations scaled by bulk quantities or equivalently turbulent intensity increase (cf Fig. 6c) below $y/H = 0.4$ and marginally reduce above $y/H = 0.4$. The location of the peak in the turbulence intensity, which correlates to the location of maximum turbulence production, shifts away from the wall for the VEF. The corresponding peak for NF is at $y^+ \approx 15$ (Zhang et al., 2015) or equivalently $y/H \approx 0.05$, which is almost the first measurement point of our PIV and hence, cannot be fully captured at the resolution that we use. This results in the false visual impression that the streamwise turbulence intensity is maximum at the wall for NF, where it should have been zero. The wall-normal velocity fluctuations decrease (cf Fig. 6d) in VEF causing an increased anisotropy as has been almost universally observed (Gyr and Bewersdorff, 2013) for drag-reducing turbulent flows. Increase in the streamwise fluctuations with polymer additives is a characteristic of the low drag reduction regime as proposed in Warholic et al. (1999) whereas, for high drag reduction, streamwise fluctuations reduce and the location of the peak is shifted further away from the wall. Thus, the turbulent fluctuations are predominantly streamwise, as also seen by the joint Probability Distribution Function (PDF) of the fluctuating streamwise and wall-normal velocity in Fig. 7 (at a near wall location $y/H = 0.095$). The higher streamwise alignment of the major axis of the joint PDF for VEF in Fig. 7b compared to NF in Fig. 7a clearly indicates that the turbulent fluctuations are preferentially streamwise. In other words there is less momentum transferred towards the walls, which is equivalent to drag reduction.

3.2. Particles in Newtonian flow

3.2.1. Drag modulation

Fig. 8 shows the change in drag (cf Eq. (3)) for varying volume fraction ϕ of particles in a NF at $Re_{2H} = 10700$. The drag increases with increasing ϕ. The solid line shows the change in drag that can be predicted by an effective suspension viscosity, obtained from the Eilers fit (Stickel and Powell, 2005); this empirical formula relates the effective viscosity to the nominal volume fraction ϕ in the limit of vanishing inertia,

$$\frac{\eta_e}{\eta} = \left(1 + \frac{\frac{5}{4}\phi}{1 - \frac{\phi}{0.65}}\right)^2. \tag{4}$$

The effective viscosity η_e is used to compute an effective Reynolds number $Re_e = U_{Bulk} 2H/\eta_e$, in turn used to find the effective friction factor from Eq. (1). This is then compared with a single phase

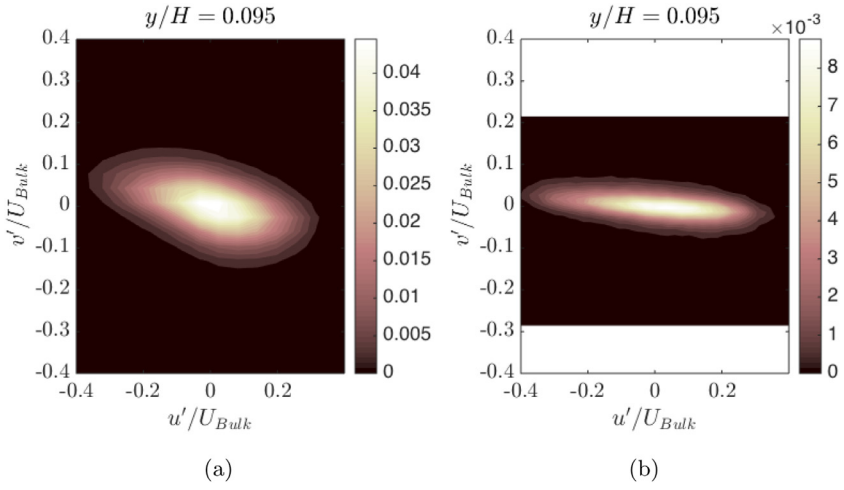

Fig. 7. Joint probability distribution function of (a) single phase NF, (b) VEF at $y/H = 0.095$. The joint PDF has been normalized such that the sum of the PDF is equal to 1.

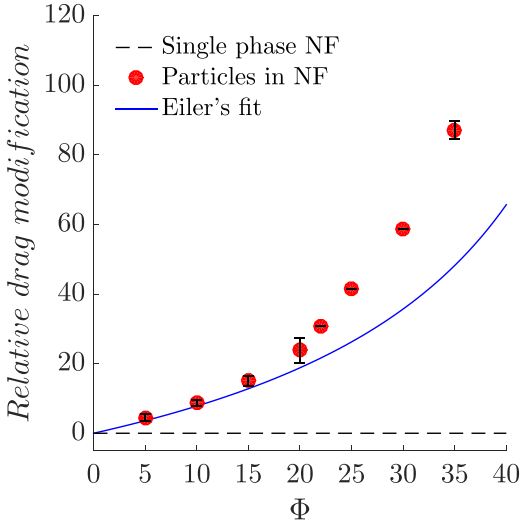

Fig. 8. Relative drag modification versus particle volume fraction ϕ in Newtonian fluid (NF) at $Re_{2H} = 10700 \pm 150$.

NF having the viscosity of the suspending solution η. This simple approach predicts an increase in the drag with the particle concentration, although of different magnitude than that observed experimentally. The prediction is closer to the experimental values for low $\phi \leq 10\%$ and diverges substantially with increasing ϕ. Abbas et al. (2017) studied a laminar flow of concentrated non-colloidal particles ($\phi = 70\%$) and used the notion of effective viscosity, based on the local particle concentration to explain the observed pressure drop. Also, recently, Bakhuis et al. (2018) found a net drag increase for an increase in ϕ in a different geometry, Taylor–Couette flow, at very high Re. However, the increase was much smaller than predicted by the increase in effective viscosity due to the particles. From the above examples, it is clear that the pressure drop cannot be correctly estimated using an effective viscosity formulation corresponding to the nominal ϕ and perhaps, spatial variation in ϕ needs to be considered in the spirit of Costa et al. (2016) who proposed scaling laws for the mean velocity profile of the suspension flow. These authors also calculated an equation able to predict the increase in drag as a function of the particle size and volume fractions in a channel flow. Their theory assumes that the flow domain can be split into two regions: (i) a region close to the wall where the difference between the mean velocity of the two phases is substantial and (ii) a region away from the wall, where the mean flow is well represented by the continuum limit of a Newtonian fluid with an effective viscosity.

3.2.2. Velocity statistics

Fig. 9a shows the mean fluid streamwise velocity for different ϕ in NF. The ratio of maximum velocity U_{Max}, at the center of the duct $y/H = 1$, to U_{Bulk} increases as ϕ increases. It is known that in the single phase turbulent regime, with decreasing Re_{2H} the ratio U_{Max}/U_{Bulk} increases due to reduced cross-stream mixing. Thus, increasing ϕ modifies the streamwise velocity profile in a way similar to the reduction of Re_{2H}. From the velocity profile, it appears that the mean streamwise velocity gradient increases with increasing ϕ which suggests that the contribution of fluid viscous stress $\mu_f dU/dy$ to the overall stress increases with increasing ϕ, at least in the plane of the wall-bisector.

The particle velocity profile in Fig. 9b exhibits a large apparent slip velocity in the near-wall region. This value in the near-wall region is most likely over-estimated because we could not measure the rotational velocity of the particle and the PTV measurement assumes that the entire particle is translating with the velocity of the centroid. This is also the reason why the particle velocity is displayed only from one particle radius away from the wall, i.e. around $y/H = 0.1$. In the flow, however, the particle also rotates, more in regions of higher shear rate, and hence the slip velocity will be lower in the near-wall region than that shown in Fig. 9b. Away from the walls, the particle rotation is lower due to lower shear rate and the estimate of the mean velocity is closer to the true value. The particle mean streamwise motion closely follows the fluid mean streamwise motion away from the near-wall region.

The particle concentration distribution profile in Fig. 9c shows characteristic maxima at the center as well the presence of a particle-rich layer near the wall as previously observed (Costa et al., 2018; Fornari et al., 2016). At $\phi = 5\%$, the particles are nearly uniformly distributed with a very weak indication of local maxima. With increasing ϕ, particles tend to migrate preferentially towards the core. This could be due to inertial shear-induced migration as explained in Fornari et al. (2016) or/and due to imbalance in the normal stresses in the wall-normal direction as seen in Lashgari et al. (2016). The local undulations in the concentration profile, especially for the highest $\phi = 20\%$, occurs due to particle layering, are visible due to the rather large size of our particles ($2H/d_p = 10$).

The fluctuations in the fluid velocity at different ϕ are shown is shown in Fig. 10. The streamwise turbulence intensity is shown

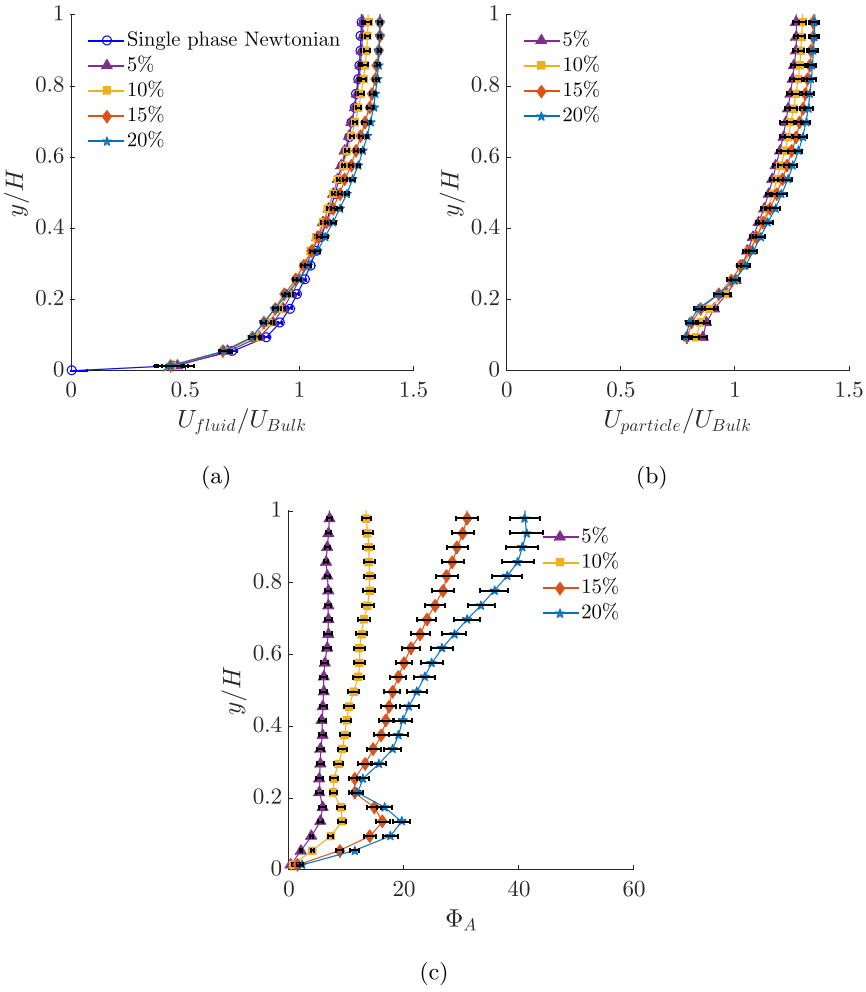

Fig. 9. Particle-laden Newtonian fluid: Mean stream-wise velocity profiles for (a) fluid phase and (b) particle phase. The particle (area) concentration profile is shown in (c).

in Fig. 10a. The inadequate resolution, as mentioned before, leads to a spurious high value of the turbulence intensity at the wall. Nevertheless, the values at higher y/H clearly indicate a reduction in the streamwise velocity fluctuations in a statistically significant sense. For $\phi = 5$ and 10%, compared to the single phase NF case, the streamwise velocity fluctuations marginally increase above the wall-normal location $y/H \approx$ 0.2 while they decrease below $y/H \approx$ 0.2. Such a behaviour was also observed, albeit more pronounced, in Fornari et al. (2018a) at $\phi = 5$ and 10%. With further increase in ϕ, the streamwise velocity fluctuations reduce for all wall-normal locations in our study. Contrarily, in Fornari et al. (2018a) the turbulence intensity at $\phi = 20\%$ increases in an intermediate region in between the wall region and the core. We believe that the above differences are consistent with the larger turbulence attenuation caused by our larger particles ($D/d_p = 10$) compared to the smaller particles ($D/d_p = 18$) in the simulations. Also, the smaller Reynolds number $Re_{2H} = 5600$ in their simulations (refer to Fornari et al. (2018a)) compared to $Re_{2H} = 11{,}000$ in the present study may lead to differences.

The wall-normal fluctuations (cf Fig. 10b) are lower in magnitude as compared to their streamwise counterpart for single phase NF flow. With addition of particles, these wall-normal fluctuations further reduce, monotonically with ϕ. The reduction near the core is substantial and, noticeably, the peak value remains nearly constant for all ϕ. This damping of the wall-normal velocity fluctuations in the core region further indicates reduction of turbulence by particles in that region.

The primary Reynolds shear stress, shown in Fig. 10c, reduces with increasing ϕ in the near wall region ($y/H \leq 0.2$), meaning that the correlation between fluid streamwise and wall-normal velocity reduces with increasing particle concentration. This can be explained by the disruption of coherent near-wall structures, responsible for the peak in single-phase flow, by the particle-rich near-wall layer. It can be noted that for low $\phi = 5$ and 10%, the primary Reynolds shear stress marginally increase above $y/H \approx$ 0.2. As also mentioned in Bakhuis et al. (2018), one can speculate that particles up to a certain ϕ introduce wakes i.e. coherent flow structures in the mean flow leading to an increase in the correlation between fluid streamwise and wall-normal velocity. However, with increasing ϕ, the wakes from particles will interact with one another resulting in reduced correlation. At the highest $\phi = 20\%$, the lower Reynolds shear stress (Fig. 10c) and lower mean streamwise velocity gradient (Fig. 9a) may cause lower production of the streamwise velocity fluctuations as seen in Fig. 10a.

Turbulent square duct flow exhibits secondary flow of Prandtl's second kind, driven by gradients in the turbulence-stresses, especially the secondary Reynolds shear stress and the second normal stress difference (Gavrilakis, 1992). These secondary motions, in the form of four pairs of counter-rotating vortices located at the duct corners act to transfer fluid momentum from the center of the duct to its corners, thereby causing a bulging of the streamwise mean velocity contours toward the corners. The strength of this secondary flow is weak, generally between 1 to 4% of the bulk velocity in most straight ducts with non-circular cross-section,

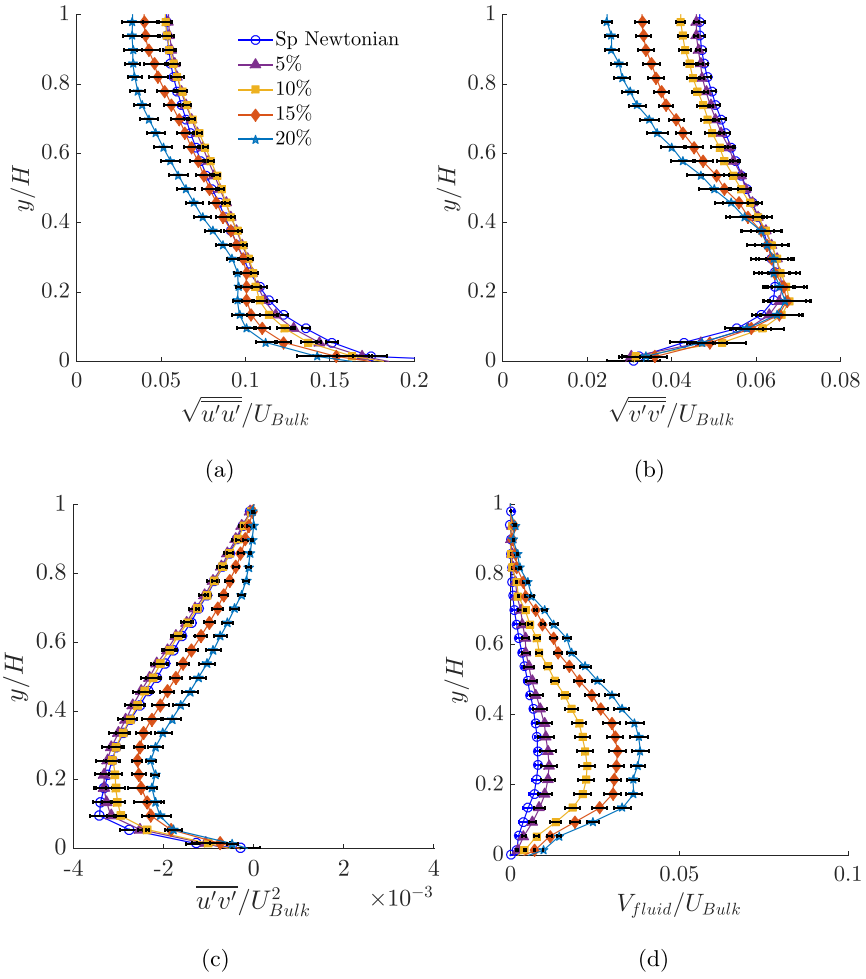

Fig. 10. Particle-laden Newtonian fluid: Fluid velocity fluctuations in the (a) stream-wise direction and (b) wall-normal direction and (c) Reynolds shear stress. Panel (d) depicts the mean wall-normal velocity. Sp stands for Single phase.

and hence prone to larger measurement uncertainties. Fig. 10d shows the mean wall-normal velocity profile, originating due to the secondary flow, in the plane of the wall-bisector $z/H = 0$. With increasing ϕ, the magnitude of the secondary flow progressively increases, at least in the plane of the wall-bisector. Fornari et al. (2018a) associated the increased secondary flow with the larger gradient in the second normal stress difference as well as fluid-particle momentum exchange for $\phi = 5$ and 10% for their smaller particles. However, at $\phi = 20\%$, they observed a reduction in the mean secondary flow, contrary to our observation. Thus, it appears that the modulation of secondary flow depends on the particle size and it continues to increase with ϕ, up to a certain ϕ which is a function of particle size.

3.3. Particles in drag reducing flow

In the following sections, we report the data for particles in a VEF at nearly the same Re_{2H} as in the NF cases described previously.

3.3.1. Change in drag

Similar to Fig. 8, Fig. 11 shows the drag change as a function of ϕ, now for particles in a VEF. The corresponding drag change for particles in a NF is also shown for comparison. As in NF, the drag increases with increasing ϕ, and nearly approaches the value corresponding to single phase NF at the highest ϕ = 20%. Fig. 11 also shows the linear fit for both types of suspending fluid. Clearly, the rate of drag increase with ϕ is higher for suspension in VEF. As mentioned before, Murch et al. (2017) and Einarsson et al. (2018) have already observed reduced particle

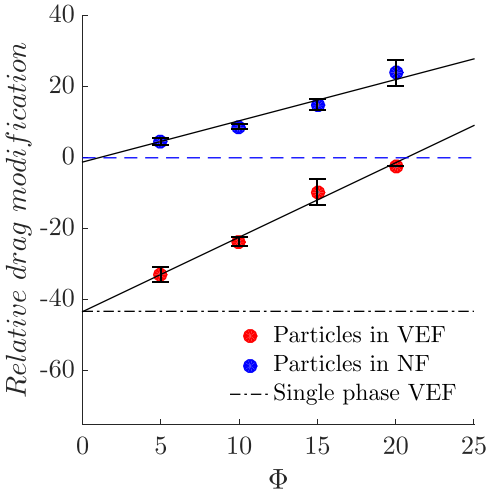

Fig. 11. Relative drag modification versus particle volume fraction for both Newtonian (NF) and viscoelastic fluid (VEF) at nearly the same Re_{2H}. For NF, $Re_{2H} = 10700 \pm 150$ and for VEF, $Re_{2H} = 11100 \pm 130$.

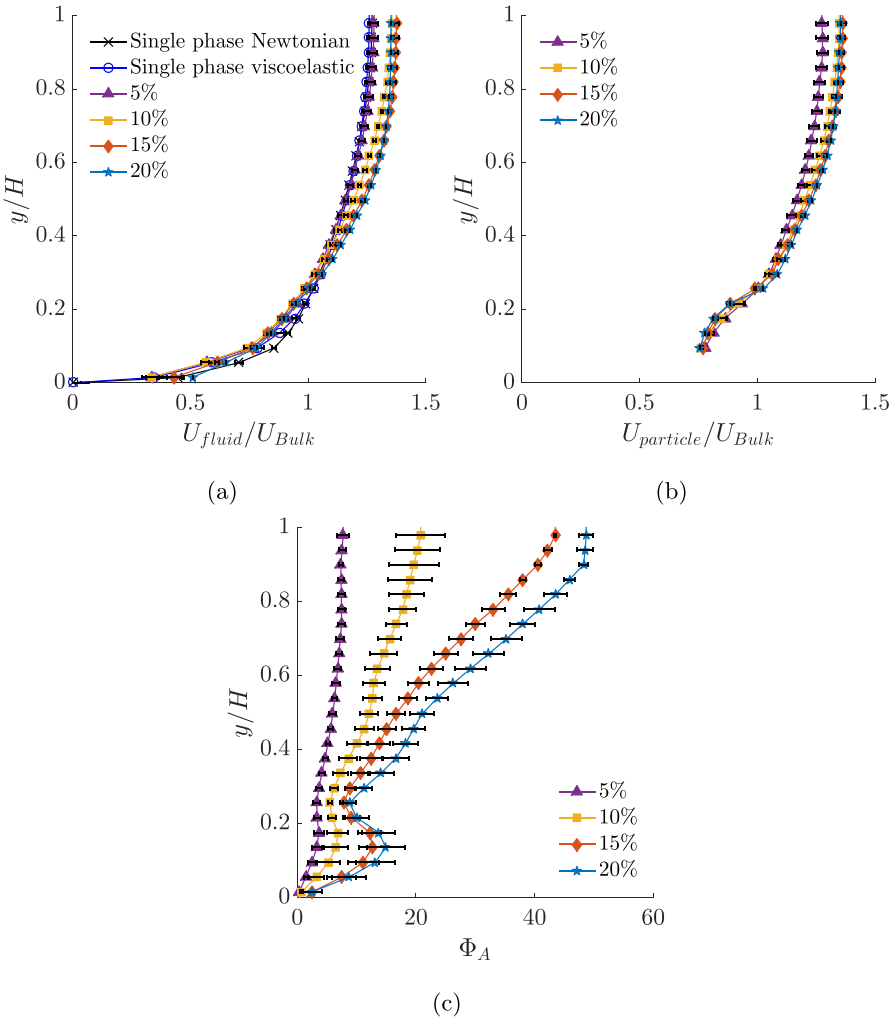

Fig. 12. Particle-laden viscoelastic fluid flow: Mean stream-wise velocity profiles for (a) fluid phase and (b) particle phase. Panel (c) depicts the particle (area) concentration profile.

Table 1
Relative drag modification versus particle volume fraction, at approximately same flow rate and particle size, for Newtonian (NF) and viscoelastic fluid (VEF).

Cases	ϕ = 0%	5%	10%	15%	20%
VEF, $2H/d_p$ = 10, Re_{2H,η_S} = 29800 ± 300	−26	−14	−2	+15	+25
NF, $2H/d_p$ = 9, Re_{2H,η_S} = 27,195 (from Zade et al., 2018)	0	−1	−0.5	–	+8

mobility and shear thickening due to elastic effects, which may hint towards a possible explanation for the higher rate of drag increase.

As mentioned before, the change in drag, as represented in Fig. 8, is calculated according to Eq. (3). For fluids with shear-dependent viscosity, the drag reduction due to polymer additives is often expressed in terms of the relative change in the friction factor compared to the Newtonian case at the same flow rate (Gyr and Bewersdorff, 2013; Owolabi et al., 2017), instead of the same Re_{2H}. This is equivalent to calculating the drag change at a constant Reynolds number Re_{2H,η_S}, based on the solvent viscosity η_S. The Re_{2H,η_S} for the VEF, now based on η_S is 29800 ± 300, and compared to single phase NF at the same Re_{2H,η_S}, the drag is 26% lower. Table 1 shows the relative change in drag caused by addition of particles compared to single phase NF at the same flow rate. It can be seen that the drag for $\phi >$ 10% in VEF is higher than the single phase NF. It is worth noting that in our previous study Zade et al. (2018), in NF with slightly larger particles ($2H/d_p$ = 9) at a slightly lower Re_{2H,η_S} = 27,195 (cf Table 1), we observed a negligible change in drag at ϕ = 5 and 10% compared to single phase NF. For ϕ = 20%, the drag increase was around 8%, which is still less than the 25% increase that we observe in VEF for the present case. This higher level of drag increase for particles in VEF compared to NF is relevant from an engineering perspective as it shows that for increasing particle concentration at constant flow rate, addition of polymer may not result in lower pressure drop (or pumping power), compared to particles in Newtonian fluids.

3.3.2. Velocity statistics

Fig. 12a and b shows the mean streamwise velocity profiles for the fluid and particle phase in the plane of the wall-bisector z/H = 0. The profile for single phase NF is also shown for comparison. As seen previously for NF, addition of particles makes the fluid velocity profile less flat i.e. the ratio U_{Max}/U_{Bulk} increases. In contrast with the NF, particles at ϕ = 15% result in the maximum U_{Max}/U_{Bulk}. The particle mean streamwise velocity $U_{particle}$

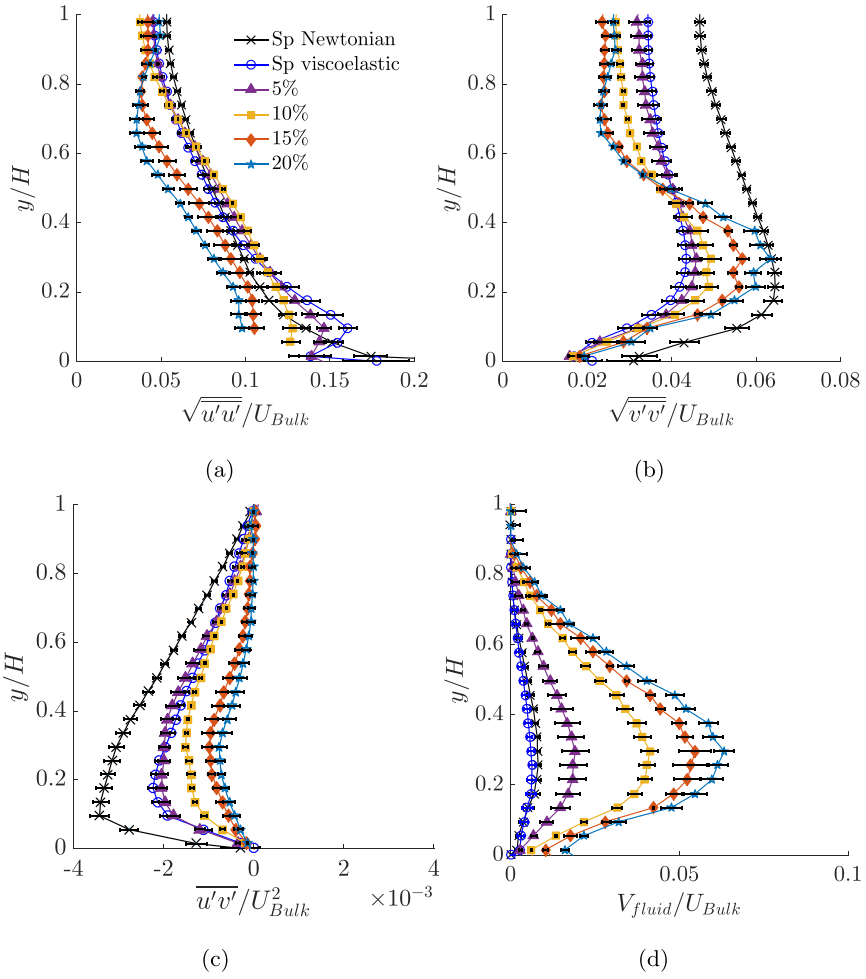

Fig. 13. Particle-laden viscoelastic flow: Fluid velocity fluctuations in the (a) stream-wise direction and (b) wall-normal direction. Panels (c) shows the Reynolds shear stress and (d) shows the mean wall-normal velocity. Sp stands for Single phase.

closely follows the fluid velocity U_{fluid} except in the near-wall region as seen for the NF. The particle area concentration profile is shown in Fig. 12c and similar to the Newtonian case, particles migrate towards the core and also form a layer of high concentration at the wall. However, the migration towards the core is substantially higher than in the NF and the migration towards the wall is marginally lower (cf Fig. 9c). This will be discussed later after looking at the fluctuating velocity statistics.

Streamwise velocity fluctuations are shown in Fig. 13a together with the single phase NF is also shown. Similar to the NF case, the streamwise turbulence intensity, generally, decreases with increasing ϕ. For $\phi = 5$ and 10%, there is a small increase between $0.2 \leq y/H \leq 0.6$. At $\phi = 10\%$, the peak value is damped and it becomes less distinct as compared to $\phi = 5\%$. Values closest to the wall have not been plotted for higher $\phi = 10$–20% due to larger uncertainties in their measurement. Away from the wall, streamwise fluctuations reduce with increasing ϕ. However, closer to the center, increasing ϕ from 10 to 20% marginally increase the fluctuations, which is not observed for the Newtonian case.

The wall-normal fluctuations exhibit a peculiar behaviour compared to the Newtonian case. As shown in Fig. 13b, these fluctuations progressively increase below $y/H \approx 0.4$ and decrease above it. Fluctuations are stronger in the region of lower particle concentration (see Fig. 12c). The peak value of these fluctuations increase with ϕ and for $\phi = 20\%$, it is very similar to the NF cases (see Fig. 10b). Interestingly, profiles for $\phi = 20\%$ in both Newtonian and viscoelastic fluids appear quite similar suggesting that at high enough ϕ, fluid wall-normal velocity fluctuations are dominated by the particle dynamics. In VEF flow, the transfer of energy from the streamwise to the wall-normal velocity fluctuations (through pressure-strain redistribution) is inhibited. This leads to reduced wall-normal fluctuations (Walker and Tiederman, 1990). The increase in wall-normal fluctuations below $y/H \approx 0.4$ in Fig. 13b may be due to an enhanced particle-induced transfer of energy from the streamwise fluctuations.

The primary Reynolds shear stress scaled by U_{Bulk}^2 also decreases with increasing ϕ for all y/H except for the lowest $\phi = 5\%$, where there is a small increase above $y/H = 0.3$ as also seen in the NF case. For the highest $\phi = 20\%$, the Reynolds shear stress reaches very small values indicating poor correlation between the streamwise and wall-normal fluctuations and their reduced contribution to the fluid momentum transport.

The mean secondary flow velocity seems to increase with ϕ as seen in Fig. 13d. The increase is evidently more, almost two-times, than the corresponding NF case (cf Fig. 10d). The origin of this secondary motion in particle-laden duct flows, as stated before, depends on quantities which have not been measured and hence, it is difficult to speculate the reason behind this higher increase.

4. Conclusion and discussion

We have reported and discussed experimental results concerning velocity and particle concentration distribution in the plane of the wall-bisector of a square duct. The suspension consists of

nearly neutrally-buoyant finite-sized spherical particles ($2H/d_p = 10$) in a turbulent Newtonian (NF) and viscoelsatic fluid (VEF) flow at the same Reynolds number Re_{2H}. In NF, the wall-friction or total shear stress at the wall is an increasing function of particle concentration ϕ. For $\phi \leq$ 10%, the magnitude of the friction factor is in satisfactory agreement with the friction factor estimated using an effective suspension viscosity η_e. The measured value increases more rapidly with ϕ than the estimate using η_e and thus, at $\phi = 35\%$, experiments measure a drag increase of around 90% whereas the drag estimated using η_e is only around 50% higher than single phase NF at the same Re_{2H}. This happens primarily beacuse the particles are not uniformly distributed and undergo preferential migration towards the core and the wall, resulting in a non-uniform equilibrium concentration profile as shown in Fig. 9c. As discussed in Lashgari et al. (2014), for a suspenion in Newtonian fluid flow, the total shear stress at the wall is due to fluid viscous stresses, fluid+particle turbulence stresses and particle-induced stresses. A square duct flow is non-homogeneous in the two cross-stream directions and hence, the stress balance has to be performed for the entire cross section to evaluate the contribution from each stress components to the total shear stress. Nevertheless, measurements of these components in the plane of the wall-bisector provides important insights in to the overall stress budget. From Fig. 10, it appears that the fluid turbulence is increasingly damped with increasing ϕ: the primary Reynolds shear stress is lowest at the highest ϕ. Simulations from Fornari et al. (2018a) indicate that the particle turbulent shear stress is smaller than the fluid phase across the entire cross-section, almost for all ϕ. Thus the contribution of turbulent stresses from both the phases is expected to decrease with ϕ. Fluid viscous stresses are expected to change marginally since the mean fluid velocity profile is not drastically altered compared to the single-phase case. Also, at high Reynolds number, the contribution of viscous stresses to the overall shear stress is small. Hence, the substantial increase in the total shear stress with ϕ occurs despite a reduction in the turbulent stresses, and hence, it is attributed to higher particle-induced stresses. Especially near the core, for $\phi = 20\%$, local particle concentration reaches values as high as 40% and one can expect that the relative contribution of the particle-induced stresses is highest in this region. Particle-induced stresses are also high in the region of the particle wall layer where there is significant slip between the two phases, as also seen in Lashgari et al. (2016). To note, the particle-induced stresses contains contributions from the hydrodynamic stresslet, particle acceleration, and inter-particle collision (Zhang and Prosperetti, 2010).

For the VEF, migration towards the core is more pronounced as can be seen in Fig. 14, where the top half reports concentration profiles for the NF case and the bottom half for the VEF case. The relatively higher particle concentration in the core for the VEF case leads to a higher contribution of particle-induced stresses towards the total stress. This could explain why the rate of drag increase is higher for VEF as compared to NF as seen in Fig. 11. Even then, the absolute value of drag is still lower for particles in VEF than NF indicating that drag-reduction due to viscoelastic effects still influence the momentum transport, at least up to $\phi = 20\%$.

Another interesting difference in the turbulence characteristics between VEF and NF can be seen from the profiles of the Reynolds shear stress compared in Fig. 15. When scaled by U^2_{Bulk}, the Reynolds shear stress for single phase VEF (lower half of Fig. 15) is lower than the corresponding NF (upper half of Fig. 15) and it reduces further with increasing particle concentration ϕ. For the highest $\phi = 20\%$, the turbulent shear stress in VEF is substantially smaller than the corresponding NF due to the combined action of particles and elasticity of the suspending media.

Better understanding from a stress perspective can be obtained by plotting the Reynolds shear stress scaled by the average friction velocity u^2_τ, as shown in Fig. 15b. An interesting note is that, when scaled with the friction velocity, the Reynolds shear stress for single-phase viscoelastic fluid appears slightly higher than that for the single-phase Newtonian fluid in Fig. 15b. This is in contrast to what is observed in channel (see Warholic et al., 1999) or pipe (see Ptasinski et al., 2001 and Choueiri et al. (2018)) flow, where the Reynolds shear stress, scaled with the friction velocity, always reduces (lower for higher drag reduction) compared to the Newtonian case. We believe this is an effect of the geometry considered in this study, a square duct, where the total shear stress along the wall-bisector has contribution from not only the viscous component dU^+/dy^+ and primary Reynolds shear stress $\overline{u'v'}^+$ but, also from the mean secondary flow. All these terms needs to be accounted for to correctly represent the linear variation of the total stress from the center of the duct towards the wall, along the bisector. Also, in our flow, the Reynolds shear stress is not as severely suppressed as near maximum drag reduction. When scaled with U^2_{Bulk}, the Reynolds shear stress is clearly lower for viscoelastic fluid as compared to Newtonian fluid as seen previously in Fig. 6b and also in Fig. 15. Nevertheless, nearly for all ϕ, the Reynolds shear stress is more suppressed for VEF than NF, indicating lower contribution of turbulent stresses to the total stress budget. Despite this larger suppression of turbulence, the rate of increase in total stress is higher for VEF due to the higher particle-induced stresses when increasing the volume fraction ϕ.

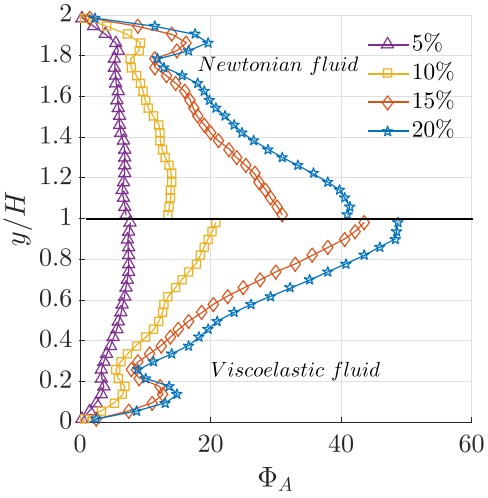

Fig. 14. Particle concentration in the plane of the wall-bisector for particle-laden Newtonian and drag reducing fluid flow.

Polymer degradation alters the rheological properties of the suspending medium and hence, strongly influences the drag reduction. Since drag reduction is directly related to the state of turbulence, the velocity statistics will change with polymer degradation. It is well known that in single phase viscoelastic fluid flow, the suppression of Reynolds shear stress and wall-normal fluctuations would reduce with higher polymer degradation. To have consistent results, hence, the data presented here have been acquired when the drag reduction has reached a nearly constant value. It is expected that the particle migration towards the core would be more pronounced with a less degraded polymer solution and thereby, the ensuing higher particle-induced stresses in the core would cause the friction factor to rise with particle concentration even faster than it has been seen in this study (refer Fig. 11).

Finally, it may be speculated that at high enough ϕ, turbulence would be highly suppressed, so that the turbulent stresses would have a negligible contribution to the total shear stress. In such a suspension, the flow would most likely be dominated by the particle dynamics as particles would become an increasingly important

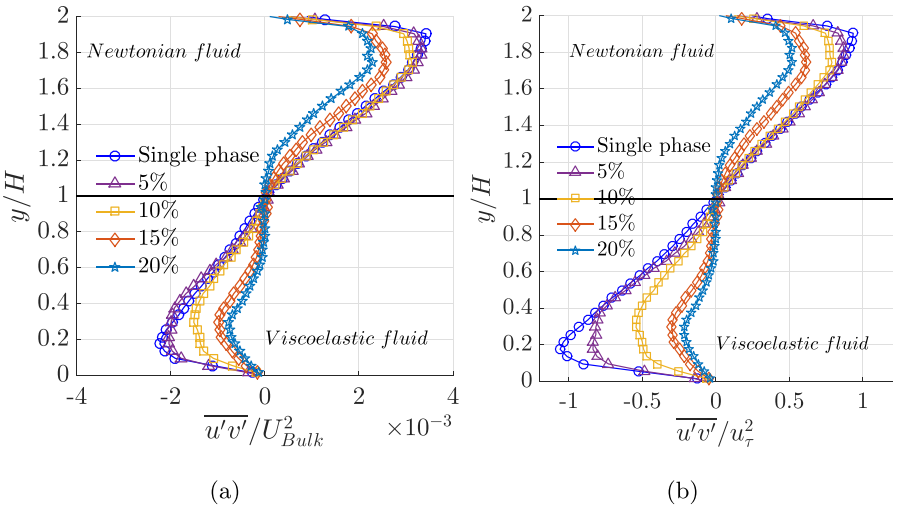

Fig. 15. Comparing Reynolds shear stress scaled using (a) U^2_{Bulk} and (b) u^2_τ in the plane of the wall-bisector for particle-laden Newtonian and drag reducing fluid flow.

carrier of momentum. With reduction in turbulence and also reduced presence of the fluid phase in the mixture, drag-reduction due to polymer additives may become increasingly ineffective. The increase in drag at such high ϕ in VEF is certainly one aspect that remains to be seen. Future work should also study the effect of particle size on the flow statistics.

Acknowledgements

This work was supported by the European Research Council Grant No. ERC-2013-CoG-616186, TRITOS, from the Swedish Research Council (VR), through the Outstanding Young Researcher Award to LB. Åsa Engström (Rise Bioeconomy AB) is gratefully acknowledged for assistance with the rheological measurements.

References

Abbas, M., Pouplin, A., Masbernat, O., Liné, A., Décarre, S., 2017. Pipe flow of a dense emulsion: homogeneous shear-thinning or shear-induced migration? AIChE J. 63 (11), 5182–5195.
Alizad Banaei, A., Loiseau, J.-C., Lashgari, I., Brandt, L., 2017. Numerical simulations of elastic capsules with nucleus in shear flow. Eur. J. Comput. Mech. 26 (1–2), 131–153.
Ardekani, M.N., Sardina, G., Brandt, L., Karp-Boss, L., Bearon, R., Variano, E., 2017. Sedimentation of inertia-less prolate spheroids in homogenous isotropic turbulence with application to non-motile phytoplankton. J. Fluid Mech. 831, 655–674.
Bagnold, R.A., 1954. Experiments on a gravity-free dispersion of large solid spheres in a Newtonian fluid under shear. In: Proceedings of the Royal Society of London A: Mathematical, Physical and Engineering Sciences, Vol. 225. The Royal Society, pp. 49–63.
Bakhuis, D., Verschoof, R.A., Mathai, V., Huisman, S.G., Lohse, D., Sun, C., 2018. Finite-sized rigid spheres in turbulent taylor–couette flow: effect on the overall drag. J. Fluid Mech. 850, 246–261.
Breugem, W.-P., 2012. A second-order accurate immersed boundary method for fully resolved simulations of particle-laden flows. J. Comput. Phys. 231 (13), 4469–4498.
Van den Brule, B., Gheissary, G., 1993. Effects of fluid elasticity on the static and dynamic settling of a spherical particle. J. Non-Newton. Fluid Mech. 49 (1), 123–132.
Burger, E., Chorn, L., Perkins, T., 1980. Studies of drag reduction conducted over a broad range of pipeline conditions when flowing prudhoe bay crude oil. J. Rheol. 24 (5), 603–626.
Byron, M.L., Variano, E.A., 2013. Refractive-index-matched hydrogel materials for measuring flow-structure interactions. Exp. Fluids 54 (2), 1456.
Choueiri, G.H., Lopez, J.M., Hof, B., 2018. Exceeding the asymptotic limit of polymer drag reduction. Phys. Rev. Lett. 120 (12), 124501.
Costa, P., Picano, F., Brandt, L., Breugem, W.-P., 2016. Universal scaling laws for dense particle suspensions in turbulent wall-bounded flows. Phys. Rev. Lett. 117 (13), 134501.
Costa, P., Picano, F., Brandt, L., Breugem, W.-P., 2018. Effects of the finite particle size in turbulent wall-bounded flows of dense suspensions. J. Fluid Mech. 843, 450–478.
Crowe, C.T., Schwarzkopf, J.D., Sommerfeld, M., Tsuji, Y., 2011. Multiphase Flows with Droplets and Particles. CRC press.
D'avino, G., Maffettone, P., 2015. Particle dynamics in viscoelastic liquids. J. Non-Newton. Fluid Mech. 215, 80–104.
Dijksman, J.A., Brodu, N., Behringer, R.P., 2017. Refractive index matched scanning and detection of soft particles. Rev. Sci. Instrum. 88 (5), 051807.
Duan, Z., Yovanovich, M., Muzychka, Y., 2012. Pressure drop for fully developed turbulent flow in circular and noncircular ducts. J. Fluids Eng. 134 (6), 061201.
Dubief, Y., White, C.M., Terrapon, V.E., Shaqfeh, E.S., Moin, P., Lele, S.K., 2004. On the coherent drag-reducing and turbulence-enhancing behaviour of polymers in wall flows. J. Fluid Mech. 514, 271–280.
Einarsson, J., Yang, M., Shaqfeh, E.S., 2018. Einstein viscosity with fluid elasticity. Phys. Rev. Fluids 3 (1), 013301.
Escudier, P., Smith, S., 2001. Fully developed turbulent flow of non-Newtonian liquids through a square duct. In: Proceedings of the Royal Society of London A: Mathematical, Physical and Engineering Sciences, Vol. 457. The Royal Society, pp. 911–936.
Fornari, W., Formenti, A., Picano, F., Brandt, L., 2016. The effect of particle density in turbulent channel flow laden with finite size particles in semi-dilute conditions. Phys. Fluids 28 (3), 033301.
Fornari, W., Kazerooni, H.T., Hussong, J., Brandt, L., 2018a. Suspensions of finite-size neutrally buoyant spheres in turbulent duct flow. J. Fluid Mech. 851, 148–186.
Fornari, W., Picano, F., Brandt, L., 2018b. The effect of polydispersity in a turbulent channel flow laden with finite-size particles. Eur. J. Mech. B. Fluids 67, 54–64.
Fredsøe, J., Deigaard, R., 1992. Mechanics of Coastal Sediment Transport. World Scientific.
Gampert, B., Rensch, A., 1996. Polymer Concentration and Near Wall Turbulence Structure of Channel Flow of Polymer Solutions, 237. ASME-PUBLICATIONS-FED, pp. 129–136.
Gavrilakis, S., 1992. Numerical simulation of low-Reynolds-number turbulent flow through a straight square duct. J. Fluid Mech. 244, 101–129.
Guazzelli, E., Morris, J.F., 2011. A Physical Introduction to Suspension Dynamics, 45. Cambridge University Press.
Gyr, A., Bewersdorff, H.-W., 2013. Drag Reduction of Turbulent Flows by Additives, 32. Springer Science & Business Media.
Hara, S., Tsukahara, T., Kawaguchi, Y., 2017. Experimental investigation of streamwise velocity fluctuation based on the reynolds-number dependency in turbulent viscoelastic-fluid flow. Int. J. Heat Fluid Flow 68, 281–289.
Kawata, T., Obi, S., 2014. Velocity–pressure correlation measurement based on planar PIV and miniature static pressure probes. Exp. Fluids 55 (7), 1776.
Kazerooni, H.T., Fornari, W., Hussong, J., Brandt, L., 2017. Inertial migration in dilute and semidilute suspensions of rigid particles in laminar square duct flow. Phys. Rev. Fluids 2 (8), 084301.
Klein, S., Gibert, M., Bérut, A., Bodenschatz, E., 2012. Simultaneous 3d measurement of the translation and rotation of finite-size particles and the flow field in a fully developed turbulent water flow. Meas. Sci. Technol. 24 (2), 024006.
Lashgari, I., Picano, F., Breugem, W.-P., Brandt, L., 2014. Laminar, turbulent, and inertial shear-thickening regimes in channel flow of neutrally buoyant particle suspensions. Phys. Rev. Lett. 113 (25), 254502.
Lashgari, I., Picano, F., Breugem, W.P., Brandt, L., 2016. Channel flow of rigid sphere suspensions: particle dynamics in the inertial regime. Int. J. Multiphase Flow 78, 12–24.
Leca, A., Leca, M., 1984. Drag reduction and heat transfer measurements with polyacrylamides on a model of a district heating system. In: Proc. 3rd Int. Conf. on Drag Reduction, Bristol, pp. 2–5.
Li, G., McKinley, G.H., Ardekani, A.M., 2015. Dynamics of particle migration in channel flow of viscoelastic fluids. J.Fluid Mech. 785, 486–505.

Metzner, A., Park, M.G., 1964. Turbulent flow characteristics of viscoelastic fluids. J. Fluid Mech. 20 (2), 291–303.
Michele, J., Pätzold, R., Donis, R., 1977. Alignment and aggregation effects in suspensions of spheres in non-newtonian media. Rheol. Acta 16 (3), 317–321.
Murch, W.L., Krishnan, S., Shaqfeh, E.S., Iaccarino, G., 2017. Growth of viscoelastic wings and the reduction of particle mobility in a viscoelastic shear flow. Phys. Rev. Fluids 2 (10), 103302.
Nowbahar, A., Sardina, G., Picano, F., Brandt, L., 2013. Turbophoresis attenuation in a turbulent channel flow with polymer additives. J. Fluid Mech. 732, 706–719.
Owolabi, B.E., Dennis, D.J., Poole, R.J., 2017. Turbulent drag reduction by polymer additives in parallel-shear flows. J. Fluid Mech. 827.
Picano, F., Breugem, W.-P., Mitra, D., Brandt, L., 2013. Shear thickening in non-brownian suspensions: an excluded volume effect. Phys. Rev. Lett. 111 (9), 098302.
Ptasinski, P., Nieuwstadt, F., Van Den Brule, B., Hulsen, M., 2001. Experiments in turbulent pipe flow with polymer additives at maximum drag reduction. Flow Turbul. Combust. 66 (2), 159–182.
Raffel, M., Willert, C.E., Wereley, S.T., Kompenhans, J., 2013. Particle Image Velocimetry: a Practical Guide. Springer.
Rouse, H., 1937. Modern conceptions of the mechanics of turbulence. Trans. Am. Soc. Civil Eng. 102, 463–505.
Segré, G., Silberberg, A., 1962. Behaviour of macroscopic rigid spheres in poiseuille flow part 2. experimental results and interpretation. J. Fluid Mech. 14 (1), 136–157.
Sellin, R., Ollis, M., 1980. Polymer drag reduction in large pipes and sewers: results of recent field trials. J. Rheol. 24 (5), 667–684.
Shahmardi, A., Zade, S., Ardekani, M.N., Poole, R.J., Lundell, F., Rosti, M.E., Brandt, L., 2019. Turbulent duct flow with polymers. J. Fluid Mech. 859, 1057–1083. arXiv: 1810.06364.
Sreenivasan, K.R., White, C.M., 2000. The onset of drag reduction by dilute polymer additives, and the maximum drag reduction asymptote. J. Fluid Mech. 409, 149–164.
Stickel, J.J., Powell, R.L., 2005. Fluid mechanics and rheology of dense suspensions. Annu. Rev. Fluid Mech. 37, 129–149.
Toms, B.A., 1948. Some observations on the flow of linear polymer solutions through straight tubes at large reynolds numbers. In: Proc. of In. Cong. On Rheology, 1948, 135.
Virk, P.S., 1975. Drag reduction fundamentals. AIChE J. 21 (4), 625–656.
Walker, D., Tiederman, W., 1990. Turbulent structure in a channel flow with polymer injection at the wall. J. Fluid Mech. 218, 377–403.
Warholic, M., Massah, H., Hanratty, T., 1999. Influence of drag-reducing polymers on turbulence: effects of reynolds number, concentration and mixing. Exp. Fluids 27 (5), 461–472.
White, C., Somandepalli, V., Mungal, M., 2004. The turbulence structure of drag-reduced boundary layer flow. Exp. Fluids 36 (1), 62–69.
Wiederseiner, S., Andreini, N., Epely-Chauvin, G., Ancey, C., 2011. Refractive-index and density matching in concentrated particle suspensions: a review. Exp. Fluids 50 (5), 1183–1206.
Yuen, H., Princen, J., Illingworth, J., Kittler, J., 1990. Comparative study of hough transform methods for circle finding. Image Vis. Comput. 8 (1), 71–77.
Zade, S., Costa, P., Fornari, W., Lundell, F., Brandt, L., 2018. Experimental investigation of turbulent suspensions of spherical particles in a square duct. J. Fluid Mech. 857, 748–783.
Zhang, H., Trias, F.X., Gorobets, A., Tan, Y., Oliva, A., 2015. Direct numerical simulation of a fully developed turbulent square duct flow up to $re_\tau = 1200$. Int. J. Heat Fluid Flow 54, 258–267.
Zhang, Q., Prosperetti, A., 2010. Physics-based analysis of the hydrodynamic stress in a fluid-particle system. Phys. Fluids 22 (3), 033306.